

Precision Multi-Mode Microwave Spectroscopy of Paramagnetic and Rare-Earth Ion Spin Defects in Single Crystal Calcium Tungstate

Elrina Hartman, Michael E Tobar, Ben T McAllister, Jeremy Bourhill, and Maxim Goryachev
Quantum Technologies and Dark Matter Labs, Department of Physics, University of Western Australia, 35 Stirling Highway, Crawley, WA 6009, Australia.^{a)}

(Dated: 23 October 2024)

We present experimental observations of dilute ion spin ensemble defects in a low-loss single crystal cylindrical sample of CaWO_4 cooled to 30 mK in temperature. Crystal field perturbations were elucidated by constructing a dielectrically loaded microwave cavity resonator from the crystal. The resonator exhibited numerous whispering gallery modes with high Q -factors of up to 3×10^7 , equivalent to a loss tangent of $\sim 3 \times 10^{-8}$. The low loss allowed precision multi-mode spectroscopy of numerous high Q -factor photon-spin interactions. Measurements between 7 to 22 GHz revealed the presence of Gd^{3+} , Fe^{3+} , and another trace species, inferred to be rare-earth, at concentrations on the order of parts per billion. These findings motivate further exploration of prospective uses of this low-loss dielectric material for applications regarding precision and quantum metrology, as well as tests for beyond standard model physics.

Scheelite, or calcium tungstate (CaWO_4), has seen a significant rise in interest for its potential of application in a myriad of contexts from test of fundamental physics, communications, and quantum computing when considered in conjunction with spin ensemble dopants such as Gd^{3+} , Er^{3+1-8} , Yb^{3+9} , Nd^{3+10} and $\text{Pr}^{3+11-13}$, with particular interest in utilizing rare-earth ions for quantum information storage and processing, and on-chip sensing^{14,15}. The scintillating dielectric also plays a key role in detection of rare events such as neutrino-less double β -decay¹⁶, radioactive decay of very long-living isotopes¹⁷ and searches for weakly interacting massive particles (WIMPs), a candidate for Dark Matter (DM)^{18,19}. The question of interest is whether or not either or both of these application avenues can be realised in a single crystal architecture at low temperatures, and what effects do the residual impurity spin ensemble defects display. To that end, this report presents the findings of precision multi-mode microwave electron spin resonance (ESR) spectroscopy, as developed in²⁰, to identify the paramagnetic residual impurities present in a high-purity CaWO_4 sample that was purchased from SurfaceNet.

The manufacturer grew the sample in the $\langle 100 \rangle$ orientation such that the a -axis of the crystal unit cell was aligned with the z -axis of the macroscopic cylindrical geometry. The sample was then placed into a metallic cavity to form a dielectrically loaded cavity resonator as shown in Fig. 1. ESR studies allowed us to measure the crystal field parameters, Landé g factors (g_L), zero field splittings (ZFS), and coupling rate (g), allowing the defect ion concentration to be calculated. The dielectrically loaded cavity was suspended in a superconducting magnet bore at the mixing chamber plate, reaching a base temperature of 30 mK when loaded in a dilution refrigerator as shown in Fig. 2. Two coaxial antennae were in-

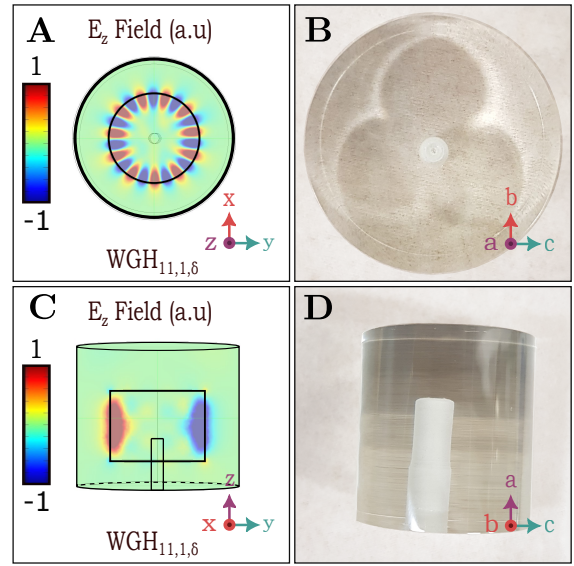


FIG. 1. The CaWO_4 crystal was grown along the $\langle 100 \rangle$ axis so that the c -axis aligned with the cylinder radial-axis, with a central hole drilled on one face of the cylinder for the purpose of mounting the crystal on a post. Here (A) and (C) show the schematics of the dielectrically loaded resonator, and the electric-energy density of the E_z field of the quasi-TM $\text{WGH}_{11,1,\delta}$ mode, calculated using COMSOL. Corresponding top (B) and side view (D) photographs of the dielectric sample are also shown. The borehole that appears white in the photograph is in a region of low field density for a WGM so frequency perturbations due to the presence of the sapphire post are negligible.

serted at the base of the cavity to allow excitation of high- Q Whispering Gallery Modes (WGM)²¹. Further coaxial cabling connected the antennae to a room-temperature Vector Network Analyser (VNA) with a high stability H-maser as the frequency reference, for microwave excitation and readout. The probes were inserted to a depth adjusted for under-coupling so that the intrinsic losses of the dielectric could be measured²². Input power

^{a)}Electronic mail: To whom correspondence should be addressed: michael.tobar@uwa.edu.au elrina.hartman@research.uwa.edu.au

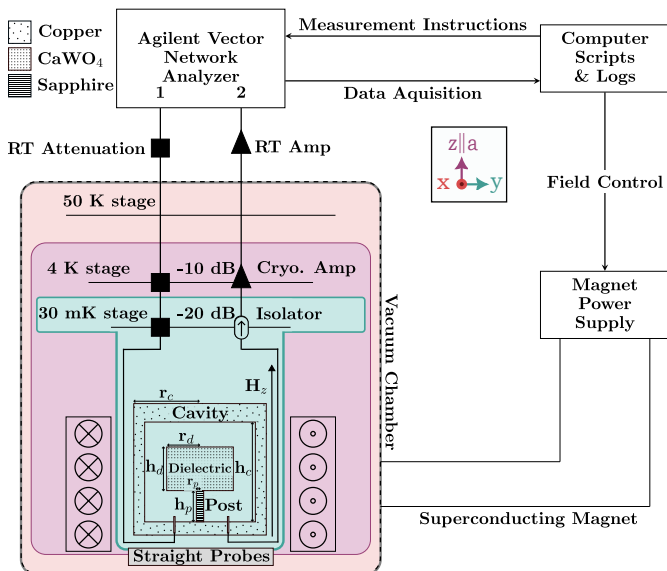


FIG. 2. The CaWO_4 crystal ($r_d = 14.68$ mm, $h_d = 20.00$ mm) was mounted on a sapphire post ($r_p = 1.75$ mm, $h_p = 14.5$ mm) clamped inside an oxygen-free copper cavity ($r_c = 25.0$ mm, $h_c = 40.0$ mm), cooled to 30 mK using a dilution refrigerator. A Vector Network Analyser (VNA) referenced by a H-maser probed the microwave resonances, automated via computer scripts that set the parameters such as scan rate, power input, magnetic field strength, and frequency span.

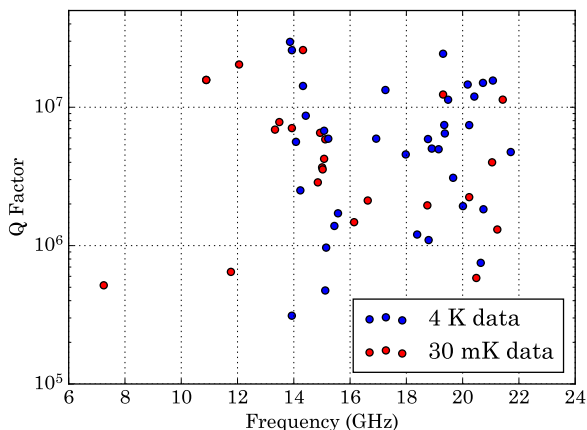


FIG. 3. This sample exhibits high mode density. Shown is the zero-field distribution of high- Q resonances at liquid helium temperature (blue). A spread of resonances were selected and remeasured at 30 mK (red), with additional lower- Q modes at lower frequencies for resolving ZFS.

was attenuated at the 4 K and 30 mK stage to reduce thermal noise from the input port. The fridge was first cooled to 4 K to assess the mode population in the crystal. Specific modes were not identified within the spectrum, however, note that WGMs are all characteristically high- Q ($Q > 10^5$)^{20,23,24}, which distinguishes them from both spurious and copper cavity modes. Further-

more, when conducting finite element modelling of the system in COMSOL Multiphysics, we find that the only high- Q modes predicted are WGMs. This is due to their coherent field distribution, an example of which can be seen in Fig. 1. A subset of these modes was then re-measured at 30 mK with trade-off considerations made between highest Q -factor and evenly spaced frequency intervals as selection criteria. Between 4 K and 30 mK there was a small frequency shift and slight reduction in Q -factor. Both effects had negligible impact on the sensitivity of the WGM ESR. A far more consequential temperature effect was the increase in spin population occupying the ground state at 30 mK. A DC magnetic field was applied along the z -axis of the cylindrical sample and ramped slowly in steps of 1 mT, tuning the spin transition via the Zeeman effect, so they would interact with high- Q WGMs. Transmission spectra of each mode were recorded at all magnetic field values so the interactions could be captured, including impacts on the photon mode's frequency, Q -factor, and transmission power. The forward power gain transfer function, specified by the scattering-parameters (S_{21}), was measured via the VNA and modelled as a Breit-Wigner distribution or asymmetric Fano resonance, given by²⁵;

$$|S_{21}| = 1 - \frac{(q\Gamma_p/2 + \Delta)^2}{(\Gamma_p/2)^2 + \Delta^2}, \quad (1)$$

where q is the Fano parameter measuring the ratio of resonant scattering to background scattering, Γ_p is the photonic resonance line-width, and Δ is the frequency detuning ($f - f_0$). The Q -factors of the modes can be calculated from the line-widths and are shown for zero DC magnetic field in Fig. 3. The best Q -factors in the crystal are of order of 3×10^7 close to 14 GHz, indicating a loss tangent of order $\tan\delta \approx 3 \times 10^{-8}$. The exact values of the anisotropic loss components could be verified more precisely using the WGM technique^{20,26-28} in a different sample, which has the cylindrical z -axis aligned with the c -axis in future studies.

In order to measure the spin transitions within the crystal, we excited them using multiple high- Q WGMs between 7 to 22 GHz. When the energy of a spin transition matches the energy of an injected WGM, they interact allowing the spin transition to be observed^{29,30}. The modes were tracked simultaneously as the magnetic field strength was increased. The resulting mode-map is plotted in Fig. 4, and as will be discussed in more detail below, g_L and ZFS were extracted from this data (see Tab. I). These two parameters take unique values for a paramagnetic defect in a given host, and thus comparing observed g_L and ZFS values to previous measurements of doped CaWO_4 allowed for the identification of some of the paramagnetic impurities within our crystal.

The energy of the spin ensembles are modelled using a spin Hamiltonian that takes into consideration the Zeeman splitting, the crystal field, and the hyperfine splitting due to spin-orbit coupling. On the scale of GHz, spin-orbit coupling was not elucidated by the data, as

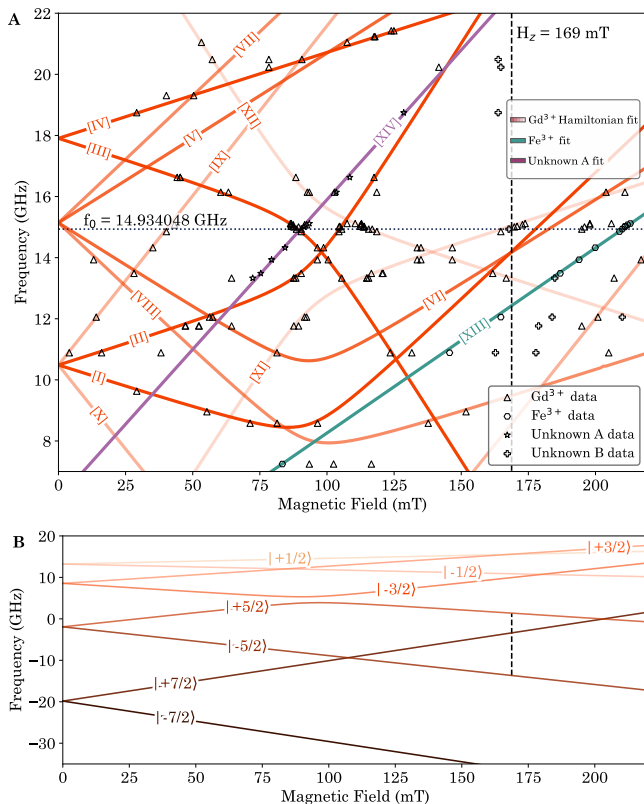


FIG. 4. **A** Shown are the perturbation sites in the frequency to magnetic field parameter space across the span of all WGMs employed. Spin transitions in $\text{CaWO}_4:\text{Gd}^{3+}$ (orange curves, labelled I to XII) are derived from the spin Hamiltonian (see equation 2). The Fe^{3+} transition is shown in green ($g_L = 4.3$, ZFS = 2.20 GHz, labelled XIII) and another unidentified paramagnetic impurity defect species ($g_L = 7$, ZFS = 6.1 GHz, labelled XIV) is shown in purple and denoted “Unknown A” data. Additional perturbations with no clear regression-line can be seen at higher field and are designated as “Unknown B” data. **B** Plotted is the $\text{CaWO}_4:\text{Gd}^{3+}$ energy-level diagram in units of frequency (GHz). The high- Q WGM used to calculate coupling strength and spin concentration is highlighted with the horizontal dotted line at 14.934048 GHz and the vertical dashed line illustrates correspondence of the magnetic field location (169 mT) in **A** and the spin transition in **B**. The frequency perturbation of this spin-photon interaction is shown in more detail in Fig. 5.

the detuning resolution and the uncertainty of the detuning from the fitting is on the same order of magnitude as the hyper-fine structure constants. Thus, their contribution was neglected for the present study and our focus was to determine the crystal field zero-field splitting and the Zeeman splitting term. The value of g_L was extracted from the slopes of the Zeeman levels as a function of magnetic field. The crystal field parameters were constructed by well-defined tesseral harmonics that describe the spin energy levels. We chose the Stevens representation, which implements a spin operator basis, and determines the Stevens coefficients experimentally. Com-

parison between Fig. 4 data and Hamiltonian fits from prior literature, served to check, corroborate or eliminate potential impurity species.

The scheelite unit cell comprises two types of atom clusters, O-Ca and O-W. Whilst the the global symmetry is tetragonal, the Ca and W centered clusters present tetragonal and distorted hexagonal symmetries respectively, by the arrangement of surrounding oxygen. The tetragonal Ca cluster has symmetry isomorphic to S_4 point symmetry³¹ and is a likely occupation site for replacement by rare-earth and shell-3d transition metal impurities. Through the process of matching g_L , ZFS and other crystal field parameters we found that Fe^{3+} and Gd^{3+} were present in the sample, along with other unidentified trace rare-earth contaminants. The crystal

Species	ΔS_z	Line	ZFS (GHz)	Transition
$\text{CaWO}_4:\text{Gd}^{3+}$ $g_L = 1.99$	1	I	10.49	$ +5/2\rangle \rightarrow +3/2\rangle$
		II		$ -5/2\rangle \rightarrow -3/2\rangle$
	2	III	17.90	$ +7/2\rangle \rightarrow +5/2\rangle$
		IV		$ -7/2\rangle \rightarrow -5/2\rangle$
	3	V	15.14	$ -5/2\rangle \rightarrow -1/2\rangle$
		VI		$ +5/2\rangle \rightarrow +1/2\rangle$
	4	VII	15.14	$ -5/2\rangle \rightarrow +1/2\rangle$
		VIII		$ +5/2\rangle \rightarrow -1/2\rangle$
	5	IX	10.49	$ -5/2\rangle \rightarrow +3/2\rangle$
		X		$ +5/2\rangle \rightarrow -3/2\rangle$
		XI	0.0	$ -5/2\rangle \rightarrow +5/2\rangle$
		XII		$ +7/2\rangle \rightarrow -3/2\rangle$
$\text{CaWO}_4:\text{Fe}^{3+}$ $g_L = 4.3$	-	XIII	2.20	-
Unknown A $g_L = 7$	-	XIV	6.10	-

TABLE I. Properties of spin transitions determined from the multi-mode spectroscopy displayed in Fig. 4A. Here ΔS_z is the change in spin quantum number.

field of $\text{CaWO}_4:\text{Gd}^{3+}$ was modelled in this work by the following Hamiltonian;

$$\mathcal{H} = g_L \mu_B H_z S_z + B_2^0 O_2^0 + B_4^0 O_4^0 + B_4^4 O_4^4 + B_6^0 O_6^0 + B_6^4 O_6^4, \quad (2)$$

where O_k^j are Stevens operators, $S = \frac{7}{2}$ and $g_L = 1.99$. The crystal field parameters are; $B_2^0 = -9.215 \cdot 10^{-1}$, $B_4^0 = -1.139 \cdot 10^{-3}$, $B_4^4 = -7.015 \cdot 10^{-3}$, $B_6^0 = 5.935 \cdot 10^{-7}$, and $B_6^4 = 4.747 \cdot 10^{-7}$ in units of GHz. This Hamiltonian allows the determination of the Zeeman energy levels of Gd^{3+} in CaWO_4 , which are shown in Fig. 4B. Note, not all the energy levels are occupied or coupled to with the present setup, thus, not every energy level theoretically predicted is reflected in the experiment. The energy difference (vertical dashed line in Fig. 4B) between the allowed transitions of these levels (coloured lines) allows

one to identify the spin transitions in Fig. 4A. This result is in good agreement with the literature³² with the only discrepancy being a 3.14% increase in the value of B_2^0 which dictates the ZFS values. This is due to the difference in orientation of this sample's c-axis to that of Baibekov et.al. who use a $\langle 001 \rangle$ cut single crystal. Gd^{3+} exhibits a distinctive electronic structure with the ground and first excited state are separated by a seven photon transition³³. Occupation of states requiring a high photon number to transition to are less likely to occur. Hence, spin occupation is distributed to a greater number of excited states than would be expected at thermodynamic equilibrium when cooled to 30 mK. Time series data verify that the tuning rate of the magnetic field was sufficiently slow to avoid reading transient and heating effects at the instance of data acquisition. The results presented here are consistent with the findings in³³ where this was indeed the case. To speculate at the source of this Gd^{3+} contamination, we note that the YVO_4 sample reported in³³ also had excess Gd^{3+} ions, and is purchased from this same manufacturer, and it may be that one of their production stations was contaminated with gadolinium. The presence of Gd^{3+} may enhance both photoluminescence and thermal-luminescence of the crystal, benefitting potential bolometric and scintillating applications.

The Fe^{3+} ($g_L = 4.3$, ZFS = 2.20 GHz) transition was observed^{34,35}. Coupling to this species was too weak to fit to and hence determine the concentration. Fe^{3+} spin ensembles have been shown to have long coherence lengths³⁶ and are a promising candidate for pulsed qubit manipulations in scheelite. Another clear linear regression is present at low frequency and high magnetic field, denoted as "Unknown A". This unknown spin ensemble has low ZFS and high g_L factor, indicating that it may be a rare-earth species. While systematic comparison of measured and literature crystal field parameters and g factors was sufficient to identify Gd^{3+} and Fe^{3+} , more information will be required to confirm the identity of Unknown A. Consideration of natural abundances and further experimental investigation using other forms of spectroscopy will inform the literature review required for likely candidates. Most rare-earth dopants in scheelite and scheelite-like hosts have been characterised using a plethora of spectroscopic techniques such as Raman spectroscopy, X-ray Powder Diffraction, Absorbance and Emission Spectroscopy, VUV synchrotron emission, mass spectrometry, and laser ablation. This field of research is resource rich due to continued and growing interest in rare-earth enhancement of phosphor technologies such as La^{3+} , Ce^{3+} , Sm^{3+} , and Tb^{3+} use in scintillators, LED's, and bio-sensing or Er^{3+} and Nd^{3+} use in solid-state lasers. Therefore, efforts to identify Unknown A are ongoing, but in a manner that prioritises preserving the single-crystal sample so as to push the frontier of these rare-earth applications in the dilute case. Other residual perturbation sites, simply designated as "Unknown B" are shown with no clear trend or regression to allow

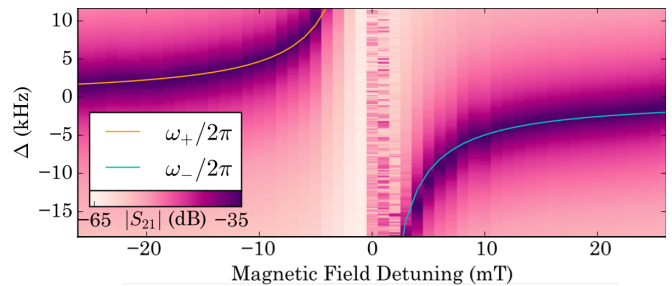


FIG. 5. Density plot of the mode interaction between a Gd^{3+} defect transition, and the 14.934048 GHz WGM at 169 mT. The fit from Eq. (3) is overlaid allowing calculation of the coupling between the photon and the spin of, $g = 1.12 \pm 0.34$ MHz, with a measured Q -factor of the WGM of 6.5×10^6 and half bandwidth of $\Gamma_p/2 = 1.14$ kHz, so $\Gamma_p \ll 2g$.

identification. More data in this region of the perturbation map is need to elucidate these contributions to the spectra.

To estimate the concentration, we analysed an interaction between a Gd^{3+} ion defect transition, and the 14.934048 GHz WGM at 169 mT, as highlighted in Fig. 4 and shown in more detail in Fig. 5, which may be modelled as a coupled harmonic oscillator, with ω_+ and ω_- as the normal mode eigensolutions to the characteristic equation³⁷⁻⁴⁰,

$$\omega_{\pm} = \frac{1}{\sqrt{2}} \sqrt{\omega_s^2 + \omega_p^2 \pm \sqrt{\omega_s^4 - 2\omega_s^2\omega_p^2 + 4\Delta_{ps}\omega_s^2\omega_p^2 - \omega_p^4}}, \quad (3)$$

where ω_p and ω_s represent the WGM and spin resonance frequency, and Δ_{ps} is the normalised, unitless, inductive mutual coupling³⁷ between these resonances. Here, the value of Δ_{ps} parameterises the rate of coupling g ($g := \frac{\Delta_{ps}\omega_p}{2}$). This model ignores loss, but suffices to fit the perturbation extremely well in the present study due to the fact that the photon line widths, $\Gamma_p = \frac{\omega_p}{Q_p}$, are of the order kHz, while g is of the order MHz, allowing strong off resonant perturbations of the photon normal modes due to the spins (here Q_p is the WGM Q -factor). The defect spin concentration (n) may be then derived from the rate of coupling, using the following expression;

$$g = g_L \mu_B \sqrt{\frac{\mu_0 \omega_p n \xi_{\perp}}{4\hbar}}, \quad (4)$$

where μ_B is the Bohr Magnetron, \hbar is the reduced Planck's constant, ξ_{\perp} is the perpendicular magnetic filling factor⁴⁰ ($\xi_{\perp} \approx 1$ for TM-WGMs), g_L was calculated from the data in Fig. 4, and μ_0 is the permeability of free space. Note, this assumes the concentration of spins is uniform, and n is the average concentration over the mode volume. The calculation of the defect concentration can thus be extracted by fitting equation 3 to the frequencies of the mode interaction in Fig. 5, and from this fit we estimate the concentration to be $n = 8.28 \pm 1.24 \times 10^{13} \text{ cm}^{-3}$.

This study found the presence of dilute spin ensembles in a scheelite sample, with Gd^{3+} being the dominant

species. Fe^{3+} and another unknown species “A” are also shown in the ESR spectra at much lower concentrations. This material exhibits low loss at mK temperatures of order 3×10^{-8} at 14.934048 GHz in frequency. The high- Q s of the WGMs hosted in the cylindrical sample allows one to conduct highly sensitive multi-mode spectroscopy with the capability to resolve spin-photon interactions with frequency detunings smaller than an order of magnitude below the linewidth of the photon resonances. In principle, this sets the lower bound of observable impurity concentrations on the order of parts per trillion⁴¹. The high coupling rate and high WGM Q -factor ($\Gamma_p \ll 2g$) indicate a high cooperativity. Accordingly, the presence of this dilute spin ensemble may be exploited in multiple avenues from bolometric sensing to qubit applications^{42,43} since the low concentration of spins, on the order of ppb, preserve the Q -factor of the dielectric, whilst exhibiting sensitivity to photon coupling.

ACKNOWLEDGEMENTS

This work was funded by the ARC Centre of Excellence for Engineered Quantum Systems, CE170100009, and Dark Matter Particle Physics, CE200100008. BM was also funded by the Forrest Research Foundation.

- ¹W. B. Mims. Phase memory in electron spin echoes, lattice relaxation effects in CaWO_4 : Er, ce, mn. *Phys. Rev.*, 168:370–389, Apr 1968.
- ²Bernal G. Enrique. Optical Spectrum and Magnetic Properties of Er^{3+} in CaWO_4 . *The Journal of Chemical Physics*, 55(5):2538–2549, 12 2003.
- ³S. Bertaina, S. Gambarelli, A. Tkachuk, I. N. Kurkin, B. Malkin, A. Stepanov, and B. Barbara. Rare-earth solid-state qubits. *Nature Nanotechnology*, 2(1):39–42, 2007.
- ⁴S. Bertaina, J. H. Shim, S. Gambarelli, B. Z. Malkin, and B. Barbara. Spin-orbit qubits of rare-earth-metal ions in axially symmetric crystal fields. *Phys. Rev. Lett.*, 103:226402, Nov 2009.
- ⁵S. Probst, G. Zhang, M. Rančić, V. Ranjan, M. Le Dantec, Z. Zhang, B. Albanese, A. Doll, R. B. Liu, J. Morton, T. Chanelière, P. Goldner, D. Vion, D. Esteve, and P. Bertet. Hyperfine spectroscopy in a quantum-limited spectrometer. *Magnetic Resonance*, 1(2):315–330, 2020.
- ⁶M. Rančić, M. Le Dantec, S. Lin, S. Bertaina, T. Chanelière, D. Serrano, P. Goldner, R. B. Liu, E. Flurin, D. Estève, D. Vion, and P. Bertet. Electron-spin spectral diffusion in an erbium doped crystal at millikelvin temperatures. *Phys. Rev. B*, 106:144412, Oct 2022.
- ⁷Marianne Le Dantec, Miloš Rančić, Sen Lin, Eric Billaud, Vishal Ranjan, Daniel Flanigan, Sylvain Bertaina, Thierry Chanelière, Philippe Goldner, Andreas Erb, Ren Bao Liu, Daniel Estève, Denis Vion, Emmanuel Flurin, and Patrice Bertet. Twenty-three-millisecond electron spin coherence of erbium ions in a natural-abundance crystal. *Science Advances*, 7(51):eabj9786, 2021.
- ⁸Salim Ourari, Łukasz Dusanowski, Sebastian P. Horvath, Mehmet T. Uysal, Christopher M. Phenicie, Paul Stevenson, Mouktik Raha, Songtao Chen, Robert J. Cava, Nathalie P. de Leon, and Jeff D. Thompson. Indistinguishable telecom band photons from a single er ion in the solid state. *Nature*, 620(7976):977–981, 2023.
- ⁹R. M. Rakhmatullin, I. N. Kurkin, G. V. Mamin, S. B. Orlinskii, M. R. Gafurov, E. I. Baibekov, B. Z. Malkin, S. Gambarelli, S. Bertaina, and B. Barbara. Coherent spin manipulations in yb^{3+} : CaWO_4 at x - and w -band epr frequencies. *Phys. Rev. B*, 79:172408, May 2009.
- ¹⁰C. G. B. Garrett and F. R. Merritt. PMR SPECTRA OF Nd^{3+} IN COMPENSATED AND UNCOMPENSATED CaWO_4 . *Applied Physics Letters*, 4(2):31–32, 12 2004.
- ¹¹I. B. Aizenberg, F. Z. Gil’fanov, and A. L. Stolov. Absorption and luminescence spectra of pr^{3+} : CaWO_4 monocrystals. *Soviet Physics Journal*, 9(1):29–33, 1966.
- ¹²Enrico Cavalli, Philippe Boutinaud, and Marek Grinberg. Luminescence dynamics in CaWO_4 : pr^{3+} powders and single crystals. *Journal of Luminescence*, 169:450–453, 2016. The 17th International Conference on Luminescence and Optical Spectroscopy of Condensed Matter (ICL’14).
- ¹³Tian-Shu Yang, Ming-Xu Su, Jian-Yin Huang, You-Cai Lv, Zong-Quan Zhou, Chuan-Feng Li, and Guang-Can Guo. Spectroscopic investigations of pr^{3+} : CaWO_4 at liquid-helium temperatures. *Phys. Rev. A*, 107:022802, Feb 2023.
- ¹⁴Giovanni Franco-Rivera, Josiah Cochran, Seiji Miyashita, Sylvain Bertaina, and Irinel Chiorescu. Strong coupling of a Gd^{3+} multilevel spin system to an on-chip superconducting resonator. *Phys. Rev. Appl.*, 19:024067, Feb 2023.
- ¹⁵G. Franco-Rivera, J. Cochran, L. Chen, S. Bertaina, and I. Chiorescu. On-chip detection of electronuclear transitions in the $^{155,157}\text{Gd}$ multilevel spin system. *Phys. Rev. Appl.*, 18:014054, Jul 2022.
- ¹⁶Yu.G. Zdesenko, F.T. Avignone, V.B. Brudanin, F.A. Danevich, V.V. Kobychchev, B.N. Kropivnyansky, S.S. Nagorny, V.I. Tretyak, and Ts. Vylov. Carvel experiment with $^{48}\text{CaWO}_4$ crystal scintillators for the double β decay study of ^{48}Ca . *Astroparticle Physics*, 23:249–263, 2005.
- ¹⁷C. Cozzini, G. Angloher, C. Bucci, F. von Feilitzsch, D. Hauff, S. Henry, Th. Jagemann, J. Jochum, H. Kraus, B. Majorovits, V. Mikhailik, J. Ninkovic, F. Petricca, W. Potzel, F. Pröbst, Y. Ramachers, W. Rau, M. Razeti, W. Seidel, M. Stark, L. Stodolsky, A. J. B. Tolhurst, W. Westphal, and H. Wulandari. Detection of the natural α decay of tungsten. *Phys. Rev. C*, 70:064606, Dec 2004.
- ¹⁸G. Angloher, C. Bucci, P. Christ, C. Cozzini, F. von Feilitzsch, D. Hauff, S. Henry, Th. Jagemann, J. Jochum, H. Kraus, B. Majorovits, J. Ninkovic, F. Petricca, W. Potzel, F. Pröbst, Y. Ramachers, M. Razeti, W. Rau, W. Seidel, M. Stark, L. Stodolsky, A.J.B. Tolhurst, W. Westphal, and H. Wulandari. Limits on wimp dark matter using scintillating CaWO_4 cryogenic detectors with active background suppression. *Astroparticle Physics*, 23:325–339, 2005.
- ¹⁹M.v. Sivers, C. Ciemiński, A. Erb, F.v. Feilitzsch, A. Gütlein, J.-C. Lanfranchi, J. Lepelmeier, A. Münster, W. Potzel, S. Roth, R. Strauss, U. Thalhammer, S. Wawoczny, M. Willers, and A. Zöller. Influence of annealing on the optical and scintillation properties of CaWO_4 single crystals. *Optical Materials*, 34(11):1843–1848, 2012.
- ²⁰Warrick G Farr, Daniel L Creedon, Maxim Goryachev, Karim Benmessai, and Michael E Tobar. Ultrasensitive microwave spectroscopy of paramagnetic impurities in sapphire crystals at millikelvin temperatures. *Physical Review B*, 88(22):224426, 2013.
- ²¹Andrey Matsko and Vladimir Ilchenko. Optical resonators with whispering-gallery mode-part i. *Selected Topics in Quantum Electronics, IEEE Journal of*, 12:3 – 14, 02 2006.
- ²²Daniel L. Creedon, Maxim Goryachev, Nikita Kostylev, Timothy B. Sercombe, and Michael E. Tobar. A 3D printed superconducting aluminium microwave cavity. *Applied Physics Letters*, 109(3):032601, 07 2016.
- ²³Michael T. Hatzon, Eugene N. Ivanov, Jeremy F. Bourhill, Maxim Goryachev, and Michael E. Tobar. Microwave-cavity-mode optimization by background antiresonance tuning. *Phys. Rev. Appl.*, 22:014081, Jul 2024.
- ²⁴Ben T. McAllister, Zijun C. Zhao, Jeremy F. Bourhill, Maxim Goryachev, Daniel Creedon, Brett C. Johnson, and Michael E. Tobar. Conductivity freeze-out in isotopically pure Si-28 at millikelvin temperatures. *Phys. Rev. Appl.*, 21:064002, Jun 2024.

- ²⁵Mikhail F. Limonov, Mikhail V. Rybin, Alexander N. Poddubny, and Yuri S. Kivshar. Fano resonances in photonics. *Nature Photonics*, 11(9):543–554, Sep 2017.
- ²⁶Michael Edmund Tobar, Jerzy Krupka, Eugene Nicolay Ivanov, and Richard Alex Woode. Anisotropic complex permittivity measurements of mono-crystalline rutile between 10 and 300 k. *Journal of Applied Physics*, 83(3):1604–1609, 1998.
- ²⁷J. Krupka, K. Derzakowski, A. Abramowicz, M. E. Tobar, and R. G. Geyer. Use of whispering-gallery modes for complex permittivity determinations of ultra-low-loss dielectric materials. *IEEE Transactions on Microwave Theory and Techniques*, 47(6):752–759, 1999.
- ²⁸Jerzy Krupka, Krzysztof Derzakowski, Michael Tobar, John Hartnett, and Richard G Geyer. Complex permittivity of some ultralow loss dielectric crystals at cryogenic temperatures. *Measurement Science and Technology*, 10(5):387, 1999.
- ²⁹Eisuke Abe, Hua Wu, Arzhang Ardavan, and John J. L. Morton. Electron spin ensemble strongly coupled to a three-dimensional microwave cavity. *Applied Physics Letters*, 98(25):251108, 06 2011.
- ³⁰K. Sandner, H. Ritsch, R. Amsüss, Ch. Koller, T. Nöbauer, S. Putz, J. Schmiedmayer, and J. Majer. Strong magnetic coupling of an inhomogeneous nitrogen-vacancy ensemble to a cavity. *Phys. Rev. A*, 85:053806, May 2012.
- ³¹M.V. Nazarov, B.S. Tsukerblat, E.-J. Popovici, and D.Y. Jeon. Optical lines in europium–terbium double activated calcium tungstate phosphor. *Physics Letters A*, 330(3):291–298, 2004.
- ³²E. I. Baibekov, M. R. Gafurov, D. G. Zverev, I. N. Kurkin, A. A. Rodionov, B. Z. Malkin, and B. Barbara. Coherent spin dynamics in a gadolinium-doped cawo4 crystal. *Physical Review B*, 95(6), feb 2017.
- ³³Lingfei Zhao, Maxim Goryachev, Jeremy Bourhill, and Michael Tobar. Indirect methods to control population distribution in a large spin system. *New Journal of Physics*, 19, 03 2017.
- ³⁴R Golding, M Kestigian, and William Tennant. Epr of high-spin fe3+ in calcium tungstate, cawo4. *Journal of Physics C: Solid State Physics*, 11:5041, 02 2001.
- ³⁵D.G McGavin and W.C Tennant. Epr study of high-spin ferric ion in a completely rhombic environment. fe3+ in cawo4. *Journal of Magnetic Resonance (1969)*, 61(2):321–332, 1985.
- ³⁶Jérôme Tribollet, J. Behrends, and Klaus Lips. Ultra long spin coherence time for fe3 in zno a new spin qubit. *EPL (Europhysics Letters)*, 84, 10 2008.
- ³⁷M.E. Tobar and D.G. Blair. A generalized equivalent circuit applied to a tunable sapphire-loaded superconducting cavity. *IEEE Transactions on Microwave Theory and Techniques*, 39(9):1582–1594, 1991.
- ³⁸N. C. Carvalho, M. Goryachev, J. Krupka, P. Bushev, and M. E. Tobar. Low-temperature microwave properties of biaxial yalo₃. *Phys. Rev. B*, 96:045141, Jul 2017.
- ³⁹Michael E. Tobar. *Gravitational Wave Detection and Low-Noise Sapphire Oscillators*. PhD thesis, The University of Western Australia, arXiv:2311.16426 [gr-qc], 1994.
- ⁴⁰Jeremy F. Bourhill. *Quantum Hybrid Systems in Low-Loss Crystalline Solids*. PhD thesis, The University of Western Australia, 2016.
- ⁴¹Nikita Kostylev, Maxim Goryachev, Andrey Bulanov, V. Gavva, and Michael Tobar. Determination of low loss in isotopically pure single crystal ²⁸si at low temperatures and single microwave photon energy. *Scientific Reports*, 7, 06 2016.
- ⁴²Seiji Miyashita and Bernard Barbara. How to cross an energy barrier at zero kelvin without tunneling effect. *Phys. Rev. Lett.*, 131:066701, Aug 2023.
- ⁴³Seiji Miyashita and Bernard Barbara. Sequential resonance for giant quantum oscillations above the energy barrier and its classical counterpart. *Phys. Rev. B*, 109:104301, Mar 2024.